Hot Cracking Phenomena in Welds III

Bearbeitet von
John C. Lippold, Thomas Boellinghaus, Carl E. Cross

schnell und portofrei erhältlich bei

Critical Conditions for Weld Solidification Crack Growth

Carl E. Cross, N. Coniglio, P. Schempp, and M. Mousavi

Introduction

The occurrence of solidification cracking during welding remains a little understood phenomenon, in spite of extensive studies and tests performed to evaluate and compare the relative weldability of many different alloys. From an approach often adopted in the welding community attributed to Prokhorov [1], solidification cracks are believed to form when a critical tensile strain is exceeded, specific to the alloy, assuming that the mushy-zone has limited ductility. Tensile stresses and strains normally form behind a moving weld pool as a result of solidification shrinkage and thermal contraction, as influenced by welding parameters and the degree of restraint [2–4].

The apparent loss of mushy zone ductility that results in solidification cracking is normally observed to occur over a specific temperature range that is bounded in the extreme by liquidus and solidus temperatures. The term brittle temperature range (BTR) has often been applied to this interval, reflecting upon the dramatic loss in apparent ductility. The upper bound to the BTR does not normally extend all the way to the liquidus. Nevertheless, alloys with a large solidification range will usually, but not always, display higher susceptibility to cracking. It has been argued that alloys with a large BTR will be exposed to a greater accumulated strain during cooling and thus exceed the ductility limit [5]. It has also been argued that rapid rates of straining facilitate exceeding the ductility limit [6].

The problem with applying the Prokhorov limited ductility approach to solidification cracking is that it cannot be physically linked to any cracking mechanism involving liquid rupture. Liquid rupture mechanisms have instead centered on cavitation and the conditions necessary to achieve a liquid pressure drop. Of particular interest in this regard has been the Rappaz-Drezet-Gremaud (RDG) interdendritic pressure drop model [7], where pressure drop has been related to solidification

C.E. Cross (✉)
Federal Institute for Materials Research and Testing, Berlin, Germany
e-mail: cecross@bajabb.com

shrinkage and the rate of transverse thermal strain. From RDG analysis it is found that strain rate, and not strain, is the key parameter controlling rupture.

Recent application of RDG analysis to aluminum welding has suggested that conditions for cavitation are not easily or normally achieved [8]. Alternative mechanisms for crack nucleation may involve gas pore formation, which is also initiated due to interdendritic pressure drop. In particular, gas pore formation in Al alloys requires the presence of dissolved hydrogen at levels high enough to overcome nucleation barriers. However, pre-existing pore nuclei in the form of oxide films may circumvent the need for pore nucleation altogether. None of the mechanisms for crack nucleation are very well understood at this point.

Following nucleation of a solidification crack, conditions must likewise favor crack growth if a continuous crack is to persist. An interesting outcome of recent analyses [8, 9] is that steady-state crack growth also requires a minimum transverse strain rate, as determined from a simple mass balance. Exploring the details of this mechanism, developing a model, and applying it to commercial Al alloys is the subject of this paper.

The fact that solidification cracking often manifests itself in the form of continuous centerline cracks tells us that the requirements for both crack nucleation and growth have been satisfied. But it does not tell us which event (i.e. nucleation or growth) is limiting the occurrence of cracking. For the sake of argument, it will be assumed in this analysis that crack nucleation is an easily occurring (i.e. non-limiting) event and that crack growth is the controlling factor. Determining whether or not this is assumption is valid must be the subject of future work, e.g. comparing critical strain rates needed for crack nucleation versus crack growth.

Coherency

Important to solidification cracking and models given below is the concept of coherency. Coherency is where adjacent dendrites have interconnected, either mechanically or through atomic bonding between dendrite arms. This allows for the transmission of transverse stress, needed for the initiation and growth of a crack. The coherency temperature (i.e. where coherency begins) defines the location in the mushy zone where cracks may exist. Above the coherency temperature, the liquid experiences only hydrostatic stress which may lead to porosity, but not cracks. This temperature is a unique property of the alloy and solidification conditions, and must be determined experimentally [10]. Likewise, the solid fraction interval over which coherency exists will determine the amount of solidification shrinkage experienced.

Crack Growth Model

Formulation of the model presented here is based upon the steady-state nature of weld solidification and the continuous nature of centerline crack growth. If it is assumed that a solidification crack tip grows in the mushy zone at the same speed

Fig. 1 Schematic showing liquid film (*shaded*) located at grain boundary in coherent region of weld mushy zone
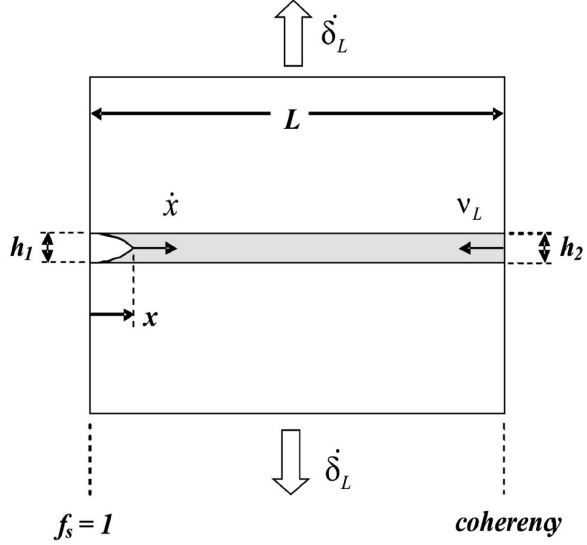
that the weld pool advances (i.e. weld torch speed), then it follows that steady-state conditions of mass flow must apply. As demonstrated in Fig. 1, the transverse displacement of a mushy zone grain boundary (δ_L) must be compensated by either advancement of the crack tip (x) or back-feeding of liquid (v_L) over an interval of time. Accordingly, the following mass balance is proposed:

$$\dot{\delta}_L(L - x) = \dot{x}h_1 + v_L h_2 \tag{1}$$

$\dot{\delta}_L$ is transverse displacement rate at the grain boundary (i.e. transverse to the direction of welding), L is length of the coherent zone (distance between coherency and solidus temperatures), x is location of the crack tip (relative to the solidus temperature), $\dot{x}$ is crack growth rate, h is liquid film thickness, and v_L is liquid flow rate.

When considering boundary conditions for the model represented by Eq. 1, the coherent zone length is found from the difference between coherent and solidus temperatures:

$$L = (T_c - T_s)/G \tag{2}$$

where G is temperature gradient. Both of these temperatures (T_c and T_s) can be measured experimentally (e.g. from thermal analysis of castings), and the weld temperature gradient can be measured from an implanted thermocouple. The position of the crack tip (x), for purposes of calculating a critical displacement rate, will be assumed small (i.e. at a fixed solid fraction, $f_s = 0.98$). In other words, we need the (L-x) term to be as large as possible to find the smallest (i.e. critical) $\dot{\delta}_L$. Crack

tip velocity is set equal to the weld travel speed [11], which is a pre-set welding parameter. Liquid film thickness is found from liquid fraction and primary dendrite spacing ($f_L \cdot \lambda$). Liquid flow rate is determined using Darcy's Equation:

$$v_L = \frac{-K}{\mu \cdot f_L} \frac{d(\Delta P)}{dx} \qquad (3)$$

where μ is viscosity and K is permeability expressed as a function of dendrite spacing [12]:

$$K = \frac{\lambda^2(1 - f_S)^2}{8\pi} \qquad (4)$$

Permeability is a measure of the openness of the dendritic structure, reflecting upon the ability of liquid to flow and feed shrinkage. ΔP represents the liquid pressure drop, with contributions from both thermal strain (ΔP_ε) and solidification shrinkage (ΔP_{sh}) calculated using the RDG model [7]:

$$\Delta P = \Delta P_\varepsilon + \Delta P_{sh} = (1 + \beta)\mu \int_{f_S = 0.98}^{f_S^{coh}} \frac{E(x)}{K} dx + v\beta\mu \int_{f_S = 0.98}^{f_S^{coh}} \frac{(1 - f_S)}{K} dx \qquad (5)$$

where β represents solidification shrinkage and v is the isotherm velocity. The integral is evaluated over the specific interval of interest (i.e. L-x). Required here is knowledge of the relation between temperature and distance (provided by G) and also temperature and solid fraction (obtained from experimental measurement or thermodynamic software). The function $E(x)$ contains a transverse strain rate term (transverse to the plane of the liquid film), which is expressed in terms of a displacement rate normalized to the dendrite spacing (gage length):

$$E(x) = \int f_S \dot{\varepsilon}_L dx = \int f_S \left(\frac{\dot{\delta}_L}{\lambda}\right) dx \qquad (6)$$

Thus, solutions for $\dot{\delta}_L$ can be found through an iterative process, assuming an initial value to estimate $E(x)$ and then using this to calculate ΔP and v_L (Eqs. 5 and 3), leading to a refined value for $\dot{\delta}_L$ (Eq. 1). Repeated iterations lead to convergence and a unique value for $\dot{\delta}_L$.

Strain Rate Distribution Model

Of considerable practical importance is the ability to relate grain boundary liquid displacement rate $\dot{\delta}_L$ (from model above) to the transverse displacement rate across the mushy-zone $\dot{\delta}$. This requires an understanding of how strain and strain rate are distributed between the grains in the mushy-zone. Establishing this relationship

is important because $\dot{\delta}$ can be easily and accurately measured with extensometers [13], whereas $\dot{\delta}_L$ cannot be easily determined (e.g. see, however, MISO technique [14]). Thus, this distribution model becomes the link between experiment and theory. Likewise, displacement in the HAZ near the fusion line can be readily simulated with FE analysis through continuum mechanics, whereas displacement in the mushy-zone cannot.

A particularly important aspect of this problem is to understand how mushy-zone grain size and shape affects strain rate distribution at liquid grain boundaries. The susceptibility to solidification cracking is known to be significantly reduced when large columnar grains are refined (i.e. smaller, equiaxed grains) [15]. It has been proposed for castings that this reduction in cracking susceptibility is the result of a reduced strain experienced at each grain boundary [16].

For purposes of approximation in this work, a very simple 2-D strain rate distribution model is proposed as represented in Fig. 2. Here grains are assumed to be free from curvature, arranged in a parallel array, and aligned in the direction of welding. It is assumed that the displacement rate across the mushy-zone $\dot{\delta}$ is distributed equally among N grains, partitioned between the grain boundary liquid $\dot{\delta}_L$ and the grain itself $\dot{\delta}_G$:

$$\frac{\dot{\delta}}{N} = \dot{\delta}_L + \dot{\delta}_G \tag{7}$$

The term $\dot{\delta}_G$ is comprised primarily of solidification shrinkage (~6 vol.% for Al alloys), large in comparison to any liquid pressure driven displacement as demonstrated in Ref. [8]. While it is clear that the grains themselves also contain liquid films, the grain boundaries are assumed to be coherency-free and hence will experience a higher portion of liquid displacement [17]. This also explains why solidification cracking is typically observed along solidification grain boundaries.
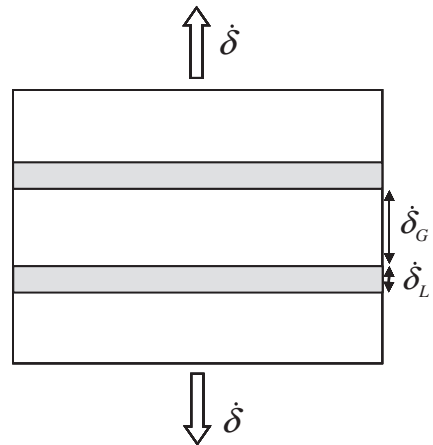
Fig. 2 Schematic showing distribution of transverse deformation rate between grains and grain boundaries in weld mushy zone

Experimental

Material

The aluminum alloys selected for examination in this study included 2219, 2014, and 2024 (aluminum association alloy designations) with compositions compared in Table 1. While all three alloys are copper bearing, they represent a wide spectrum in resistance to solidification cracking. Alloy 2219 is essentially a commercial grade Al-Cu binary alloy, high in Cu content and low in Mg, developed specifically to have good weldability in welded assemblies (e.g. Space Shuttle External Tank). Alloys 2014 and 2024 are both considered to be Al-Cu-Mg alloys, in that they can attain high strength through formation of S'-CuAl$_2$Mg precipitates. Both alloys are lower in Cu and higher in Mg than Alloy 2219 and both are generally known to have poor weldability [18], although Alloy 2014 can be welded successfully (e.g. Titan Missile casing) using a 4043 filler metal. It should also be noted that both Alloys 2014 and 2024 are much higher in Mn, Si, and Fe content than Alloy 2219 (Table 1).

Welds and Castings

Autogenous, bead-on-plate, partial penetration, gas-tungsten arc welds were made on 7 mm thick plate using the welding parameters given in Table 2. Coupon size was 23 mm wide × 140 mm long. Weld bead dimensions varied slightly with alloy and were approximately 8 mm wide × 4 mm deep. Weld metal cooling rate was measured by plunging a type-K thermocouple (0.5 mm dia.) into the moving weld pool.

Castings were made by melting 50 g samples of wrought plate, taken from the same plate used to make weld coupons. Samples were melted in a furnace held

Table 1 Measured aluminum alloy compositions for alloys examined in this study (in wt%)

Alloy	Cu	Mg	Mn	Si	Fe
2219	6.42	0.02	0.23	0.06	0.17
2014	5.13	0.46	0.74	0.90	0.24
2024	4.66	1.42	0.69	0.09	0.18

Table 2 Gas-tungsten arc welding parameters used to make autogenous, partial penetration, bead-on-plate welds for microstructure and thermal analysis

|	
Arc polarity	Direct current, electrode negative (DCEN)
Arc current	160 A
Arc voltage	18 V
Torch travel speed	4.0 mm/s
Shielding gas	Ar-He (50/50)

at 750°C and then cast into a cylindrical graphite mold (19 mm dia. × 60 mm length) coated with boron-nitride. Metal was poured into the top of the cylinder, while at the bottom of the cylinder there was a heat sink made from stainless steel (80 mm dia. × 30 mm thick) used to promote directional solidification. Cooling curves and temperature difference measurements were obtained from type-K thermocouples (0.25 mm dia.) pre-placed along the cylinder centerline, and calibrated with 99.999% pure Al. One thermocouple was placed at the bottom of the cylinder, and another placed 3 mm directly above it.

Both welds and castings were cross-sectioned and prepared for metallographic examination. Specimens were mounted, ground, and polished to 1 micron and examined at 500× and 1000 × magnification in the un-etched state.

Results and Discussion

Solidification Analysis

Cast microstructures for the three different alloys are compared in Fig. 3. Based upon the observation of phases in Fig. 3 in comparison with previous analyses of cast structure [19, 20], the predominant interdendritic eutectic phase for Alloy 2219 is taken to be Al_2Cu. Whereas for Alloys 2014 and 2024 there are three distinct phases present: Al_2Cu (light grey), Mg_2Si (black), and $Al_{15}(CuFeMn)_3Si_2$ (dark grey). While these are the constituents that predominate, it is possible that there may
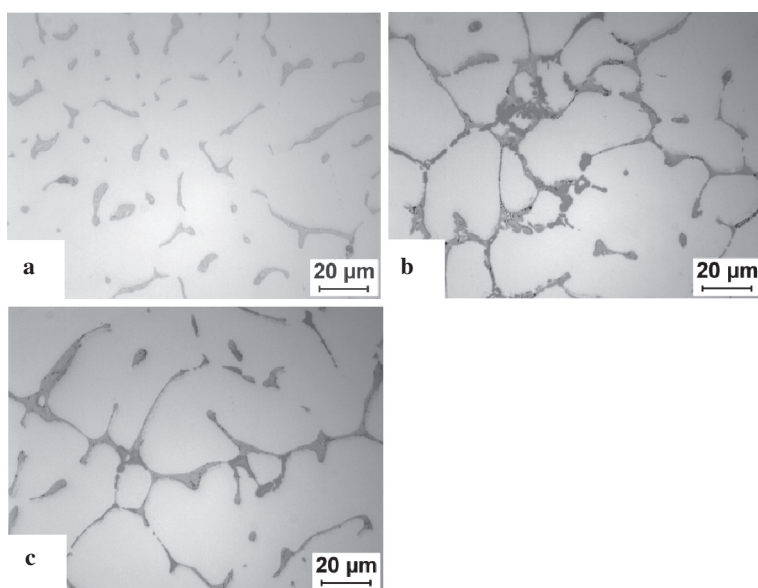
Fig. 3 Solidification microstructure for cast alloys (**a**) 2219, (**b**) 2014, and (**c**) 2024

**Table 3** Comparison of solidification phase reactions for Alloys 2219 [19] and 2024 [20]

Alloy	Reaction	Temperature (°C)
2219		
	$L \rightarrow \alpha\,(Al)$	648
	$L \rightarrow \alpha\,(Al) + Al_2Cu$	547
2024		
	$L \rightarrow \alpha\,(Al)$	637
	$L \rightarrow \alpha\,(Al) + Al_{15}(CuFeMn)_3Si_2$	613
	$L \rightarrow \alpha\,(Al) + Al_{15}(CuFeMn)_3Si_2 + Al_{20}Cu_2Mn_3$	544
	$L + Al_{20}Cu_2Mn_3 \rightarrow \alpha\,(Al) + Al_2Cu + Al_{15}(CuFeMn)_3Si_2$	
	$L \rightarrow \alpha\,(Al) + Mg_2Si + Al_2Cu$	480
	$L \rightarrow \alpha\,(Al) + Al_2Cu + Mg_2Si + Al_2CuMg$	

be smaller amounts of other phases present (e.g. S-phase or $Al_{20}Cu_2Mn_3$-phase). It is important to note that it is the minor and impurity elements (Mn, Si, Fe) that have a major effect on phase formation in Alloys 2014 and 2024.

In comparison with the simple Al-Cu eutectic for Alloy 2219, the sequence of solidification phase reactions for Alloy 2024 is shown in Table 3, with corresponding reaction temperatures, taken from Bäckerud et al. [20]. While the liquidus temperatures are similar ($T_{L/2219} = 648°C$, $T_{L/2024} = 637°C$), the terminal solidus is significantly lower for Alloy 2024 ($T_{S/2219} = 547°C$, $T_{S/2024} = 480°C$) and hence the solidification range is larger for this alloy. This is further demonstrated by comparing the temperature-vs-solid fraction curves for these two alloys shown in Fig. 4, taken from published thermodynamic software predictions [21, 22]. Here the terminal eutectic plateau for Alloy 2219 occurs near 547°C in agreement with binary equilibrium, whereas for Alloy 2024 the plateau is some 20 degrees higher than Bäckerud's measurement. It should be noted that there is more terminal eutectic generated for Alloy 2219 (13% solid fraction) than for Alloy 2024 (9% solid fraction). This, in itself, would be expected to have significant effect in aiding the feeding of shrinkage in Alloy 2219.

Shown in Fig. 5 are the results from thermal analysis of cast Alloy 2024. These curves together with similar data for Alloys 2219 and 2014 were used in the identification of the liquidus, coherency, and temperatures as summarized in Table 4. The measured liquidus and solidus temperatures for Alloys 2219 and 2024 are in approximate agreement with Fig. 4. The solidus value for Alloy 2014 is found to lie between those for Alloys 2219 and 2024. Accordingly, the solidification range ($T_L - T_S$) is seen to increase in the order 2219, 2014, 2024.

Coherency temperatures were determined using a method outlined in Ref. [23] and demonstrated in Fig. 5. Coherency is assumed to begin at the end of the α-phase plateau as indicated by the dip in the temperature difference curve (at 5 s) due to a change in heat transfer. Comparing coherency start temperatures in Table 4 shows a similar value for all three alloys (~629°C). The range of temperature over which coherency occurs (i.e. $T_C - T_S$) is thus found to increase in the order 2,219, 2,014,
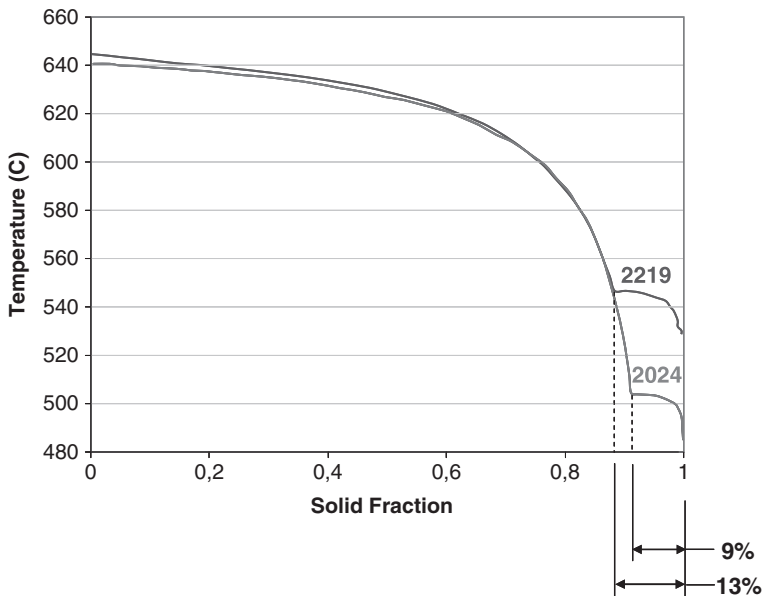
Fig. 4 Solidification curves for Alloys 2219 and 2024 based upon thermodynamic predictions, with data replotted from [21, 22]

2,024. However, when expressed in terms of solid fraction with the aid of Fig. 4, the coherency range for Alloy 2219 is actually found to be the same or larger than for Alloys 2014 and 2024 (see $1-f_s{}^c$ in Table 4).

Application of Proposed Models

The crack growth model, as represented by Eqs. 1–6, was applied using the physical constants shown in Table 5 together with the thermal and solid fraction data of Figs. 4 and 5. Figure 6 gives a comparison of the resulting critical grain boundary deformation rates $\dot{\delta}_L$ shown as a function of crack tip location x for the three different alloys. If for purposes of comparison the crack tip is assumed to be located at a solid fraction of 0.98, the critical deformation rates $\dot{\delta}_L$ are seen to be similar for all three alloys (between 0.18 and 0.22 μm/s) as compared in Table 6, with Alloy 2219 having the highest value.

When these $\dot{\delta}_L$ values at $f_s = 0.98$ are substituted into the deformation rate distribution model (Eq. 7), one is able to obtain the corresponding critical deformation rate $\dot{\delta}$ across the mushy zone assuming a variety of different grain sizes and corresponding N values. These values can in turn be converted to strain rate $\dot{\varepsilon}$ (i.e. dividing $\dot{\delta}$ by bead width) as represented by the curves in Fig. 7. Clearly these curves do not reflect the established behavior of these alloys, where Alloy 2219 should be
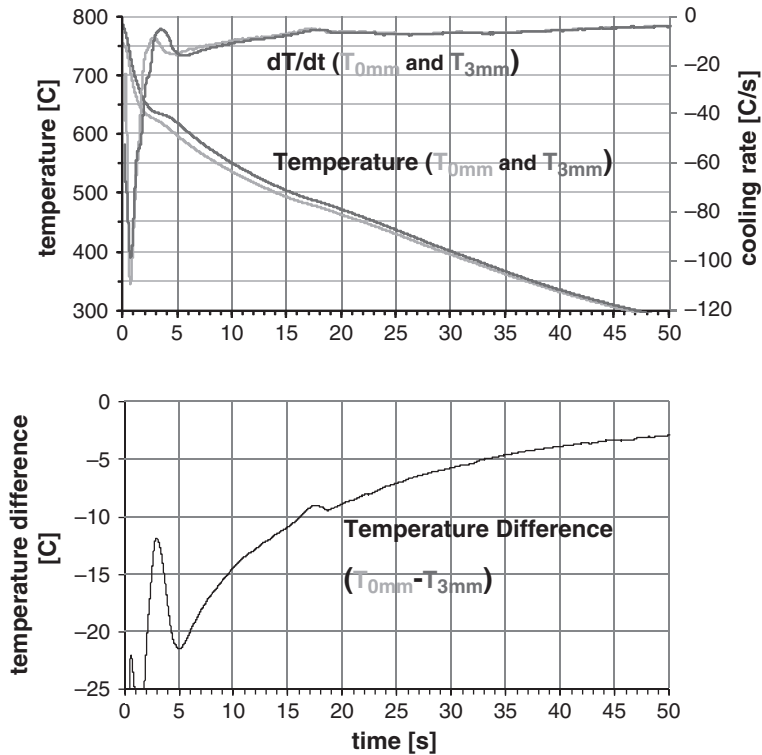
Fig. 5 Differential thermal analysis of Alloy 2219 cast specimen

Table 4 Summary of critical (liquidus, coherent, and solidus) temperatures measured from thermal analysis of castings (in ºC). Also compared are solidification temperature range (ΔT_S), coherency temperature range (ΔT_C), and coherency solid fraction range ($1 - f_s^c$)

Alloy	T_L	T_C	T_S	ΔT_S	ΔT_C	$(1 - f_s^c)$
2219	641	629	543	98	86	0.50
2014	645	629	501	134	128	0.50
2024	637	622	487	150	135	0.40

Table 5 Physical constants pertaining to aluminum used in making calculations for crack growth model

Parameter	Symbol	Value	Reference
Shrinkage factor	ß	0.06	[24]
Liquid viscosity	μ	1×10^{-3} Pa·s	[24]
Dendrite arm spacing	λ	10 μ	–
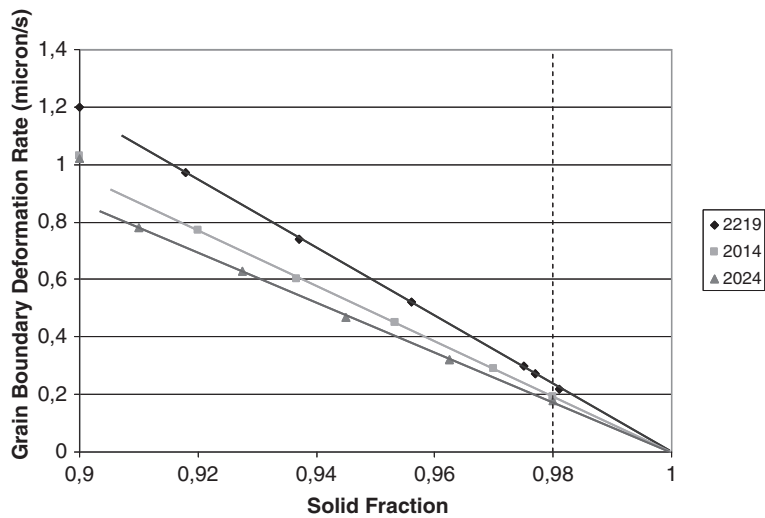
Fig. 6 Critical grain boundary deformation rates obtained from crack growth model, assuming 10 μm dendrite spacing for each alloy
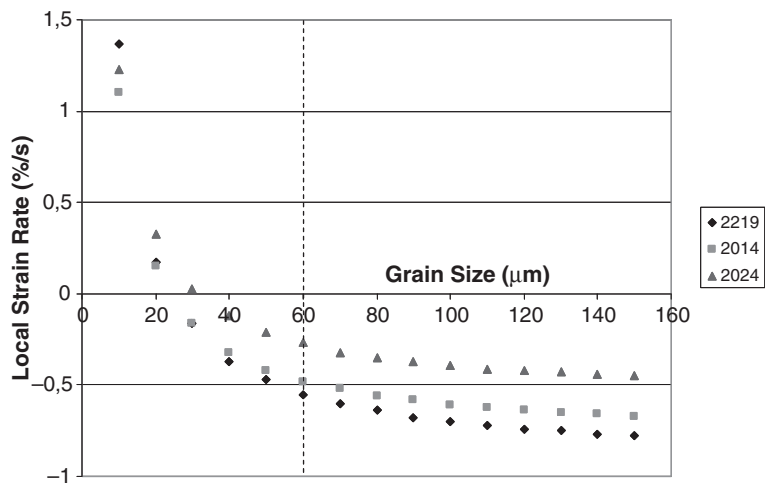
Fig. 7 Critical strain rate across mushy zone required for crack growth based upon strain rate distribution model and data from Fig. 6

expected to have the best weldability and the highest critical $\dot{\varepsilon}$ values. When comparing alloys at a normal grain size (e.g. 60 μm diameter) in Fig. 7 and Table 6, the $\dot{\varepsilon}$ value for 2219 is found to be negative which is also not to be expected. From previous experience, a $\dot{\varepsilon}$ value on the order of +0.5%/s is expected for weld metal exhibiting good weldability [25].

Table 6 Summary of critical displacement and strain rate values for solidification crack growth taken from Figs. 6–9 (assuming crack tip at $f_s = 0.98$ and grain size = 60 μm). Two sets of data are shown, one for constant λ (10 μm) and one for variable λ

Alloy	λ (μm)	$\dot{\delta}_L$ (μm/s)	$\dot{\varepsilon}$ (%/s)	λ (μm)	$\dot{\delta}_L$ (μm/s)	$\dot{\varepsilon}$ (%/s)
2219	10	0.22	−0.55	39	0.86	0.5
2014	10	0.19	−0.48	29	0.54	0.10
2024	10	0.18	−0.27	1	0.28	−0.11

In order to adjust our input to the models to obtain more realistic results, the relative permeability of the three alloys was adjusted accordingly. To achieve the desired result, dendrite arm spacing was arbitrarily selected as follows: 2219-39 μm, 2014-29 μm, 2024-16 μm. Using these adjusted values as input to the crack growth model produced $\dot{\delta}_L$ curves shown in Fig. 8 with a greater difference now observed between alloys. Specifically, when compared at $f_s = 0.98$, $\dot{\delta}_L$ is seen to vary between 0.28 and 0.86 μm/s (see Table 6). When converted to strain rate values in Fig. 9, it is observed that Alloy 2219 now demonstrates the highest weldability and has a realistic positive $\dot{\varepsilon}$ value at 60 μm grain size. Likewise, Alloy 2024 has a negative $\dot{\varepsilon}$ value at 60 μm grain size, indicative of very poor weldability.

It must be clarified that the dendrite spacing numbers arbitrarily selected above have no relation to actual values. Dendrite spacing is determined principally by cooling rate (~100°C/s for arc welds) and is typically on the order of 10 μm for most alloy arc welds. This suggests that the problem lies with the permeability formulation (Eq. 4), an observation also noted and debated by others [26]. Alloys 2014 and 2024 both contain coarse constituents, not found in Alloy 2219, that likely
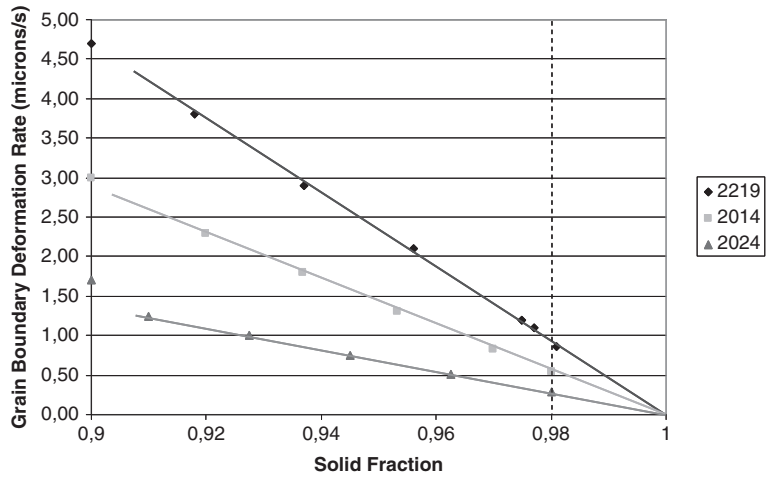
Fig. 8 Critical grain boundary deformation rates obtained from crack growth model, assuming different dendrite spacings for each alloy (2219-39 μm, 2014-29 μm, 2024-16 μm)
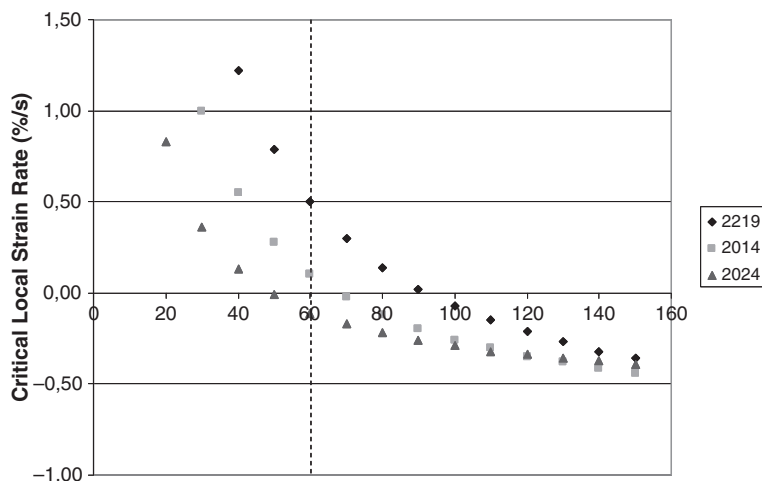
Fig. 9 Critical strain rate across mushy zone required for crack growth based upon strain rate distribution model and data from Fig. 8

serve to impede fluid flow and reduce permeability. Such intricate differences in microstructure are not accounted for in Eq. (4).

The curves of Fig. 9 suggest a significant influence of grain size on weldability. In particular, if Alloy 2219 were to be welded without filler at high heat input to get course grains of 100 μm, it could potentially experience weldability problems. Also, if Alloy 2024 could be grain refined to 30 μm grain size through use of sufficient grain refiner or current pulsing techniques, it could be made weldable according to these predictions. This fine 30 μm grain size can be achieved in arc welded Al alloys, e.g. through the use of abnormally high TiAl$_3$ additions up to 0.3 wt% Ti [15]. Likewise, the requirement to use a Si containing 4043 filler alloy in order to weld Alloy 2014 may be linked to the grain refinement attributed to Si. Si is known to produce high constitutional undercooling in Al alloy solidification favoring grain nucleation [27], which is believed to be the major factor contributing to improved weldability when using a 4043 filler [25].

Weld Microstructure

Thermal analysis and phase identification for this study was made using castings cooled at a rate of 10°C/s. This was done because identification of coarser phases is easier to accomplish and the resolution of thermal arrests on cooling curves is improved. The cooling rate for a weld, in comparison, was measured to be 110°C/s at 550°C, which results in much finer microstructures as shown in Fig. 10. Questions arise as to how much cooling rate might affect the critical temperature values in Table 4, and how this will affect model predictions. Although the thermal and phase
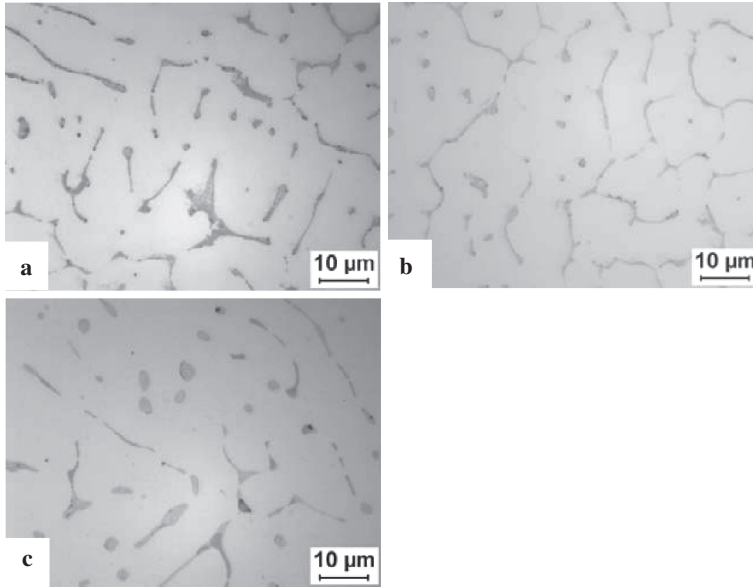
Fig. 10 Weld metal microstructures for alloys (**a**) 2219, (**b**) 2014, and (**c**) 2024

analysis of welds provides much more a challenge, work is progressing in this area [28] using single sensor thermal analysis (SSTA) specifically developed for welding [29].

Conclusion

The critical strain rate across the mushy zone needed to sustain continuous crack growth has been taken as a measure of susceptibility to solidification cracking. Two models have been proposed; one model defining the critical grain boundary displacement rate based upon a mass balance, and one model relating grain boundary displacement rate to the strain rate across the mushy zone (a measureable quantity). The former takes into account the ability to feed thermal and solidification shrinkage as controlled by permeability. Both models have been applied to three different Al-Cu (-Mg) alloys each having markedly different weldability (Alloys 2219, 2014, and 2024).

When the inherent permeability of each alloy is assumed to be the same, the models predict that Alloy 2024 should have the best weldability, which goes against common knowledge and experience. Although the coherent temperature range is greater for Alloy 2024, the corresponding solid fraction range is smaller, meaning that this alloy will experience less shrinkage over this critical solidification interval, thus leading to this result. However, it has been demonstrated that if the permeability of the dendrite structure is adjusted to reflect the better feedability of Alloy 2219 (i.e.

less constituent phases blocking dendrite channels), model predictions can be made to coincide with real-world experience. Thus, it appears to be the coarse Si, Fe, and Mn- containing constituents in Alloys 2024 and 2014 that reduce their weldability in relation to Alloy 2219.

The models have also demonstrated a strong dependence of weldability on grain size. The results suggest that grain refinement in arc welds (down to 30 μm grain size) may allow difficult alloys (e.g. Alloy 2024) to be welded free from cracking. This together with data collected previously [15] provides a compelling argument supporting the need for grain refinement in aluminum weld metal.

Considering in greater depth the application of the simple models presented here, one must concede that the problem of solidification cracking is much more complicated and multi-faceted than what has been assumed. Even so, the simple ideas presented here are congruent with observed behavior. The phenomenon of crack "healing" by backfilling represents a case in point. This is a condition often observed in weldability testing when severe strain is applied during welding (e.g. varestraint test) where pools of eutectic are observed in the form of lens-shaped features. This phenomenon may in fact not represent the healing of cracks as is usually assumed, but rather the feeding of strain and shrinkage. In fact, it is difficult to conceive how a crack could possibly form and later be backfilled in a continuous manner behind a moving weld pool (although this is quite a different matter for HAZ liquation cracks).

Another case in point is the typical smooth appearance of solidification cracks and the absence of dendrite tearing. The absence of any sign of dendrite tearing does not mean that dendrite coherency is not present. On the contrary, coherency is an absolute requirement in order to generate the transverse stress needed for cracking. The growth of cracks depends upon this transverse stress, but does not necessarily involve the tearing of dendrites. The proposed crack growth model incorporates the continuous separation of a liquid film, thus allowing for a smooth, undulating fracture surface as is normally observed.

References

1. Prokhorov NN (1956) The problem of the strength of metals while solidifying during welding. Svarochnoe Proizvodstvo 6:5–11.
2. Chihoski RA (1972) The character of stress field around a weld pool moving on aluminum sheet. Welding Journal 51:9s–18s.
3. Feng Z (1994) A computational analysis of thermal and mechanical conditions for weld metal solidification cracking. Welding in the World 33:340–347.
4. Zacharia T (1994) Dynamic stresses in weld metal hot cracking. Welding Journal 73: 164s–172s.

5. Pumphrey WI and Jennings PH (1948) A consideration of the nature of brittleness and temperature above the solidus in castings and welds in aluminium alloys. Journal Institute of Metals 75:235–256.
6. Arata Y, Matsuda F, Nakata K and Shinozaki K (1977) Solidification crack susceptibility of aluminum alloy weld metals (Report II)- Effect of straining rate on cracking threshold in weld metal during solidification. Trans JWRI 6:91–104.
7. Rappaz M, Drezet J-M and Gremaud M (1999) A new hot-tearing criterion. Metal lurgical and Materials Transactions 30A:449–455.
8. Coniglio N and Cross CE (2009) Mechanisms for solidification crack initiation and growth in aluminum welding. Metallurgical and Materials Transactions 40A:2718–2728.
9. Coniglio N and Cross CE (2008) Weld parameter and minor element effects on so lidification crack initiation in aluminum. In: Hot Cracking Phenomena in Welds II. Springer, pp. 277–310.
10. Dahle K and Arnberg L (1997) Development of strength in solidifying aluminum alloys. Acta Materialia 45:547–559.
11. Robino CV, Reece M, Knorovsky GA, DuPont JN and Feng Z (2005) Prediction of maximum crack length in longitudinal varestraint testing. In: Proceedings of the 7th International Conference Trends in Welding Research, ASM International, pp. 313–318.
12. Ganesan S, Chan CL and Poirier DR (1992) Permeability for flow parallel to primary dendrite arms. Materials Science and Engineering-A 151:97–105.
13. Kannengiesser T, McInerney T, Florian W, Böllinghaus T and Cross, CE (2002) The influence of local weld deformation on hot cracking susceptibility. In: Mathematical Modeling of Weld Phenomena-6, Institute of Materials, pp. 803–818.
14. Matsuda F, Nakagawa H, Nakata K, Kohmoto H and Honda Y (1983) Quantitative evaluation of solidification brittleness of weld metal during solidification by means of in-situ observation and measurement (Report 1)- Development of the MISO technique. Trans JWRI 12:65–72.
15. Mousavi MG, Cross CE and Grong Ø (1999) Effect of scandium and titanium-boron on grain refinement and hot cracking of aluminium alloy 7108. Science and Technology of Welding and Joining 4:381–388.
16. Spittle JA and Cushway AA (1983) Influences of superheat and grain structure on hot tearing susceptibility of Al-Cu alloy castings. Metals Technology 10:6–13.
17. Drezet J-M and Allehaux D (2008) Application of the Rappaz Drezet Gremaud hot tearing criterion to welding of aluminum alloys. In: Hot Cracking Phenomena in Welds II. Springer, pp. 19–38.
18. Cross CE, Kramer LS, Tack WT and Loechel LW (1990) Aluminum weldability and hot cracking theory. In: Weldability of Materials, ASM International, pp. 275–282.
19. Mondolfo LF (1976) Aluminum Alloys- Structure and Properties. Butter worths, London.
20. Bäckerud L, Król E and Tamminen J (1986) Solidification Characteristics of Aluminium Alloys, Vol. 1. Skanaluminium, Oslo.
21. Cao G and Kou S (2005) Liquation cracking in full-penetration Al-Si welds. Welding Journal 84:63s–71s.
22. Cao G and Kou S (2006) Predicting and reducing liquation cracking susceptibility based on temperature vs. fraction solid. Welding Journal 85:9s–18s.
23. Arnberg L, Bäckerud L and Chai G (1996), Solidification Characteristics of Aluminium Alloys, Vol. 3. Skanaluminium, Oslo.
24. Van Horn KR (1967) Aluminum, Vol. 1: Properties, Physical Metallurgy, and Phase Diagrams, ASM International.
25. Coniglio N, Cross CE, Michael Th and Lammers M (2008) Defining a critical weld dilution to avoid solidification cracking in aluminum. Welding Journal 87:237s–247s.
26. Carlson KD and Beckermann C (2009) Authors' Reply to Discussion of "Prediction of shrinkage pore volume fraction using a dimensionless Niyama Criterion". Metallurgical and Materials Transactions 40A:3054–3055.
27. Easton MA and StJohn DH (2001) A model of grain refinement incorporating alloy constitution and potency of heterogeneous nucleant particles. Acta Materialia 49:1867–1878.

28. Coniglio N, Cross CE, Dörfel I and Österle W (2009) Phase formation in 6060/4043 aluminum weld solidification. Materials Science and Engineering A 517:321–327.
29. Alexandrov BT and Lippold JC (2006) A new methodology for studying phase transformations in high strength steel weld metal. In: Proceedings of the 7th International Conference Trends in Welding Research, ASM International, pp. 975–980.